Pulse shape discrimination using EJ-299-33 plastic scintillator coupled with a Silicon Photomultiplier array

Can Liao, Haori Yang *

Department of Nuclear Engineering & Radiation Health Physics, Oregon State University, 3451 SW Jefferson Way, Corvallis, OR 97331, United States

A B S T R A C T

Recent developments in organic plastic scintillators capable of pulse shape discrimination (PSD) have gained much interest. Novel photon detectors, such as Silicon Photomultipliers (SiPMs), offer numerous advantages and can be used as an alternative to conventional photo multiplier tubes (PMTs) in many applications. In this work, we evaluate the PSD performance of the EJ-299-33 plastic scintillator coupled with a SiPM array. 2D PSD plots as well as the Figure of Merit (FOM) parameters are presented to demonstrate the PSD capability of EJ-299-33 using a SiPM as the light sensor. The best FOM of 0.76 was observed with a 1.0 MeVee (MeV-electron-equivalent) energy threshold, despite the high noise level of the SiPM array. A high-speed digital oscilloscope was used to acquire data, which was then processed offline in MATLAB. A performance comparison between two different PSD algorithms was carried out. The dependence of PSD quality on the sampling rate was also evaluated, stimulated by the interest to implement this setup for handheld applications where power consumption is crucial.

© 2015 Elsevier B.V. All rights reserved.

1. Introduction

The pulse shape discrimination (PSD) technique is based on the differences in pulse shapes of scintillation signals from fast neutron and gamma–ray interactions in organic scintillators [1]. The difference in pulse shape is commonly explained as the existence of two decay components in fluorescence emitted following an excitation. The fast main component decays exponentially during the de-excitation, while the slower component exhibits a much longer decay time yet the same wavelength. It is believed that the net result of the excitation process in an organic scintillator is the production of a population of excited molecules in the S_1 and T_1 states [2]. The fast component of the fluorescence is emitted during the transition between the S_{10} state and one of the vibrational states in the ground electronic band. In most organic scintillators, the decay time for this type of transitions is on the order of a few nanoseconds. The slow component of the fluorescence emission originates from the collision and annihilation between two molecules residing in the T_1 states, and the following transition from the formed S_1 state to the S_0 state:

$$T_1 + T_1 \rightarrow S_0 + S_1; \ S_1 \rightarrow S_0 + light \tag{1}$$

The decay time of this component is then determined by the lifetime of the T_1 states and the rate of T_1–T_1 collisions and is usually much longer than that of the fast main fluorescence. Energetic recoil protons produced from neutron interactions create a much higher concentration of triplets than recoil electrons from gamma interactions, because of their larger linear energy transfer (LET) and shorter range. Thus, the scintillation signals from neutron events exhibit a much more prominent slow component. This difference in proportions of the fast and slow components of fluorescence serves as the basis for the PSD technique [3,4].

Liquid organic scintillators have been widely used for PSD. However, they are not suitable for many field applications due to potential leakage and fire hazard. Although good PSD performance of liquid scintillators suggests that crystallographic structure is not crucial to the triplet–triplet annihilation mechanism, plastic scintillators have traditionally presented poor PSD properties. Previous studies suggested that the excitation traps formed by a lower band-gap fluorescence impurity are the cause of this [5]. Recent breakthrough in the development of plastic scintillators with good PSD performance has gained much interest because of the dramatically improved stability over organic liquids [6].

Optical readout of scintillators is typically achieved using traditional photomultipliers (PMTs). Recently developed solid state photomultipliers (SSPMs) offer numerous advantages, including high photon detection efficiency, high gain, small size, improved robustness, low operation voltage, low cost and immunity to magnetic fields [7]. As one of the most popular variants of SSPMs, the Silicon Photomultipliers (SiPMs) consist of a high-density matrix of diodes, which are operated in limited Geiger–Muller mode, providing gain at the level of 10^6 [8].

* Corresponding author. Tel.: +1 541 7377057.
  E-mail address: haori.yang@oregonstate.edu (H. Yang).

PSD of fast neutrons and gamma-rays is critical for measurements in a mixed radiation field for nonproliferation, safeguards and homeland security applications [9–11]. However, its implementation has been often limited by the scintillation detector material or the optical sensor. In this study, we present our effort to improve the deployability of the PSD technique by addressing both aspects. In particular, our work demonstrated PSD capability with an Eljen EJ-299-33 plastic scintillator coupled with a SensL ArraySB-4 SiPM array, despite the much higher inherent noise and longer response time in such SSPMs.

Digital PSD using fast waveform digitizers has been proved to be a very promising technique. In our study, output signals from the SiPM evaluation board were digitized directly without any analog shaping. The entire pulse processing was performed in the digital domain on a PC. The PSD performance of the system was quantified by the introduction of a Figure of Merit (FOM). The implemented PSD algorithms can be readily realized on a FPGA in real time. The impact of sampling rate on the PSD performance was also studied and discussed.

2. Experimental methodology

2.1. Experiment setup

The EJ-299-33 plastic scintillator sample used in this study was manufactured by Eljen Technologies. This crystal has the shape of a right circular cylinder with a diameter of 1 in. and a height of 1 in. It was mounted onto a SiPM array manufactured by SensL, model number ArraySB-4. The SiPM array is based upon a 4 by 4 arrangement. Each pixel has an active area of 3×3 mm^2 and is mounted in a low-profile ceramic package. Such package permits close packing on all four sides, enabling the best fill factor available in a commercial unit with only 200 μm dead space between pixels. There are 4774 microcells in each pixel, providing a pixel gain of 3×10^6. The scintillator and the SiPM array were carefully wrapped together with Teflon tape as shown in Fig. 1. This prevented leakage of scintillation light and improved light collection in spite of the mismatch in size between the crystal and the SiPM array. The response of ArraySB-4 covers a wide spectral range from 300 nm to 800 nm [12]. The photon detection efficiency (PDE) curve peaks around 425 nm, which very well matches the emission spectrum of EJ-299-33, as shown in Fig. 2 [13].

The ArraySB-4 SiPM array was read out with a preamplifier board (Model: ArraySB4-EVB-PreAmp) mounted on an evaluation board (Model: ArraySB4-EVB-PixOut). The preamplifier board provides differential voltage outputs from each of the 16 pixels of the array. The evaluation board takes an input voltage and steps it down with a regulator to provide optimal operating voltage to the SiPM array as well as the preamplifier circuits. It also provides the user with the option to adjust the bias applied on the operational amplifiers. An external 5 V power supplier was used to power the preamplifiers board in our study for maximum dynamic range of the preamplifier. The evaluation board provides readouts for each individual pixel and a sum signal of all the 16 channels. This sum signal was used in the following PSD study. It was read out with an Agilent DSOX3104A digital oscilloscope, which has a maximum sampling rate of 5 GSPS and a resolution of 8-bit. The oscilloscope was connected to the evaluation board via 50 Ω input impedance. In the following study, pulses were acquired at 1GSPS in a 4 μs window and analyzed offline. The dynamic range of the oscilloscope was set to 5 V. Each data acquisition was triggered with a threshold of 500 mV and started at 0.5 μs before the trigger. The rising time of a typical pulse was roughly 20 ns, due to the long charge propagation time through the passive network formed by the SiPM equivalent circuit. Dark
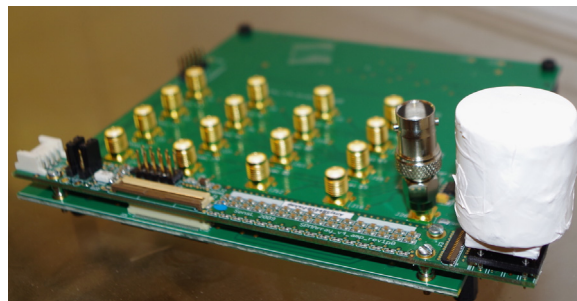

Fig. 1. The EJ-299-33 plastic scintillator coupled to a 4×4 SensL ArraySB-4 SiPM array and wrapped with Teflon tape.

noise was on the order of 25 mV, which caused fluctuation in baseline and posed a challenge on PSD. The plastic scintillator and SiPM array assembly were placed in a light-tight box painted black inside to minimize stray light. The temporal behavior of a typical pulse measured with this setup and the amplitude of signal with dark current and noise are shown in Fig. 3. All the experiments are done at a constant room temperature.

A plutonium–beryllium (Pu–Be) neutron/gamma source was used in the following measurements, providing mixed neutron and gamma radiations. Lead bricks and polyethylene blocks were used to alter the relative intensity of neutrons and gamma-rays reaching the detector.

2.2. Energy calibration

The energy calibration was performed using Cs-137 and Co-60 gamma sources. Fig. 4 shows the experimental configuration with the source and scintillator in a dark box. Due to the small size and intrinsic property of the organic scintillator, Compton scattering dominated among the interactions of gamma-rays within the detector. The pulse amplitude was calculated as the integral within a time window, which was the same as how the total charge integral was calculated in the following PSD studies. The constructed pulse amplitude distributions are shown in Fig. 5.

The energy calibration was then performed using the energy of the Compton edge in each energy spectrum. The Compton edge for an incident gamma-ray energy is given by the well-known equation:

$$E_{\mathrm{compton}} = \frac{E_\gamma}{m_e c^2 / 2E_\gamma + 1} \tag{2}$$

where, E_γ is the energy of the incident gamma-ray, and $m_e c^2$ is the rest energy of an electron. According to this equation, the Compton edge of the 662 keV gamma-rays from Cs-137 is at 477 keV. Energies of Compton edges for the 1117 keV and 1333 keV gamma-rays from Co-60 are calculated to be 963 keV and 1119 keV respectively. Due to the small detector size, the probability of multiple scattering is small. Thus, a simple energy calibration was developed by averaging the two Co-60 Compton edge values. This average energy was then assigned to the voltage amplitude where the Compton plateau reached 70% of its maximum intensity. The same procedure was implemented while calibrating using the Compton edge from the 662 keV gamma-rays emitted by Cs-137 [14,15]. Moreover, with measurements using the oscilloscope, one could obtain the zero level. Thus, there is no offset to subtract for calibration. Using the method described above, the energy calibration was obtained as shown in Fig. 6.
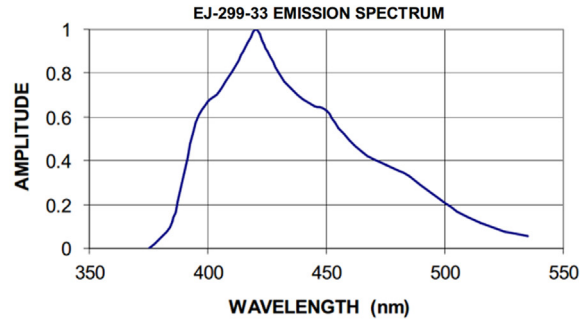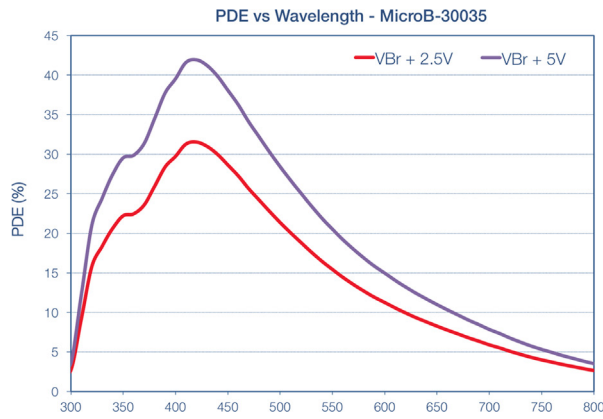
Fig. 2. PDE of the SiPM as a function of wavelength and the EJ-299-33 emission spectrum [12,13].
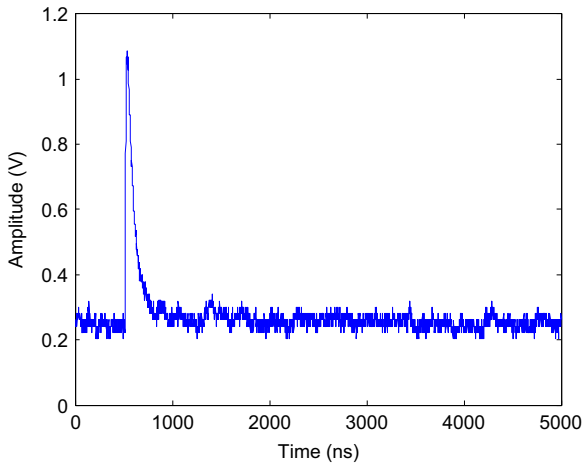

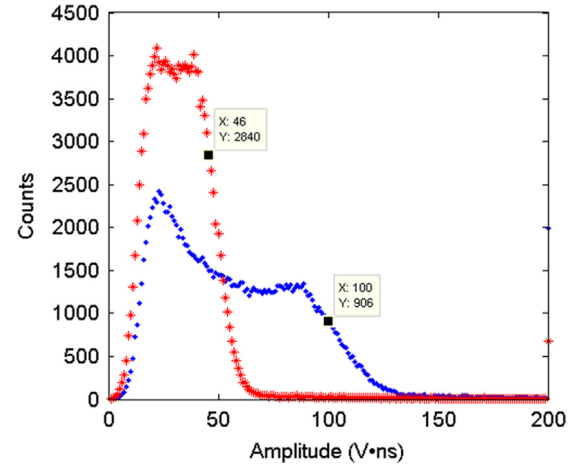**Fig. 3.** A typical pulse measured at the output of the differential preamplifier.

Fig. 5. Cs-137 and Co-60 gamma pulse amplitude distributions for energy calibration.

Fig. 4. The experimental setup for energy calibration.
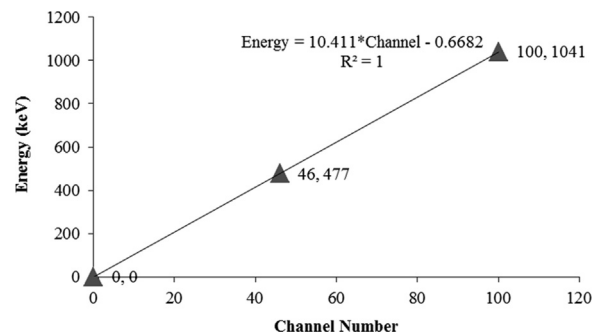

Fig. 6. Energy calibration result using Cs-137 and Co-60 gamma sources.

3. Experimental results with a PuBe neutron/gamma source

3.1. Charge comparison method

As discussed above, the scintillation signal from a particle with larger LET has a larger slow component due to T_1–T_1 collision and annihilation. Since a fast neutron pulse in the EJ-299-33 plastic scintillator actually originates from the energy deposition by recoil protons, it has a much larger tail than a gamma-ray pulse. The charge comparison method was first chosen as the method for PSD in this work [16]. In this method, each pulse is integrated via two separate routes. The first integration, A_1, the total integral, is performed from the beginning of the pulse to an optimized end point of the tail. The

second integral, A_2, taken from a certain starting position on the falling edge to the same end point as used for the total integral, is called the tail integral. The ratio of the tail integral to the total integral, R, is used to distinguish events resulting from different particles as shown in Fig. 7.

3.2. PSD results using charge comparison method

Fig. 8 shows a neutron signal and a gamma signal from the output of the preamplifier board after smoothing and normalization. The difference in signal shapes could be clearly observed. In the charge comparison method, a long integration window is usually chosen to ensure enough information about the pulse

shape is contained. However, given the large dark noise of the SiPM array, a shorter integration window was found to optimize the PSD performance. The total integral window used here was 360 ns wide and started at 50 ns before the signal reached 90% of its maximum on the rising edge. The tail integral was selected to start at 110 ns after the beginning of the total integral.

PSD results using this method are shown as 2D histograms (tail integrals vs. total integrals) for three different shielding configurations. A total of 150,000 pulses were acquired and analyzed in each case. Good separations are observed in all scenarios. In Fig. 9 (a), the lead shielding stopped a large portion of the incident
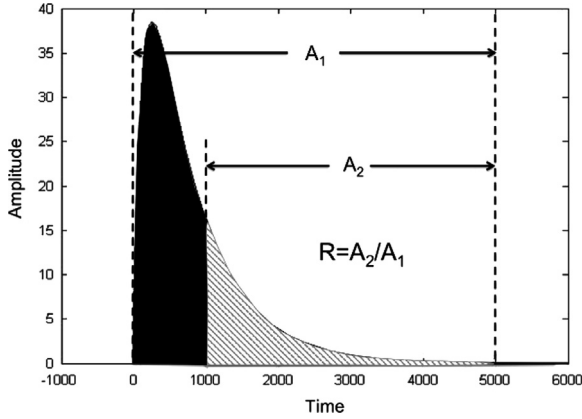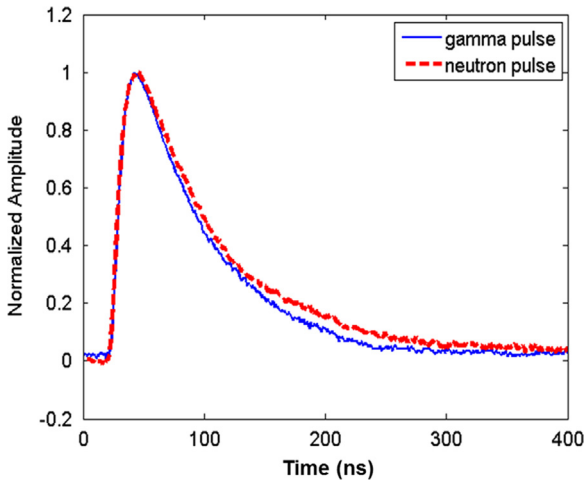
gamma-rays, thus the neutron branch is much more prominent compared to the case with no shield, as shown in Fig. 9(b). Fig. 9 (c) shows that the polyethylene shielding stopped or slowed down some of the incoming neutrons, which led to relatively less neutron counts. The changes in relative neutron and gamma-ray intensity with different shielding configurations validated the effectiveness of the PSD method.

Noticing the distortions in Fig. 9(b) and (c) at large charge integrals above 3.0 MeVee, we provide a short discussion on the cause here. The distortion could result from either the saturation of the SiPM or the saturation of the preamplifier. As the SiPM has a finite number of pixels, the maximal number of photons that can be simultaneously detected is limited, which is proportional to the output signal. This leads to a saturation behavior of the SiPM response and fundamentally limits its dynamic range. The number of pixels fired depends on the number of photons arriving at the detector as:

$$N = m \times \left(1 - e^{-\frac{\varepsilon_{PDE} \cdot N_{photon}}{m}} \right) \tag{3}$$

where, N is the number of fired pixel, m is the total number of pixels, N_{photon} is the number of incident photons and ε_{PDE} is the photon detection efficiency [18]. According to the above equation, Fig. 10 shows a plot of the number of photoelectrons ($\varepsilon_{PDE} \cdot N_{photon}$) vs. the number of pixels fired. The total number of pixels m is $16 \times 4774 = 76,384$, as given in the datasheet [12].

The light yield of EJ299-33 is 8600 photons per MeVee. The average photon detection efficiency of the SiPM used here is around 30% at the emission wavelength of EJ299-33 [12,13]. Accordingly, the maximal number of photoelectrons created is 10,320 ($=4 \times 8600 \times 30\%$) at 4 MeVee, assuming a 100% light collection efficiency. Thus, even at the maximum pulse amplitude in this experiment, the SiPM was still far from being saturated. Thus, the authors conclude that the distortions are likely due to the saturation of the preamplifier.

Fig. 11 shows the tail-to-total ratio distributions with different threshold settings, which are 0.5 MeVee, 1.0 MeVee and 1.5 MeVee. The discrimination parameter in this figure is the tail-to-total ratio. The distorted signals were rejected by setting an upper limit of 3.0 MeVee. The neutron peak and the gamma-ray peak were then fitted with two Gaussian functions. A widely used FOM was used to characterize the PSD quality [19]. Here, the FOM is defined as:

$$FOM = \frac{\Delta P}{W_1 + W_2} \tag{4}$$

where ΔP, is the separation of the peals of the two fitted Gaussian distributions. W_1 and W_2 are the full widths at half maximum (FWHM) of these two peaks respectively. As observed in Fig. 11, higher thresholds result in better FOM values, indicating that PSD performance is better at higher energies.
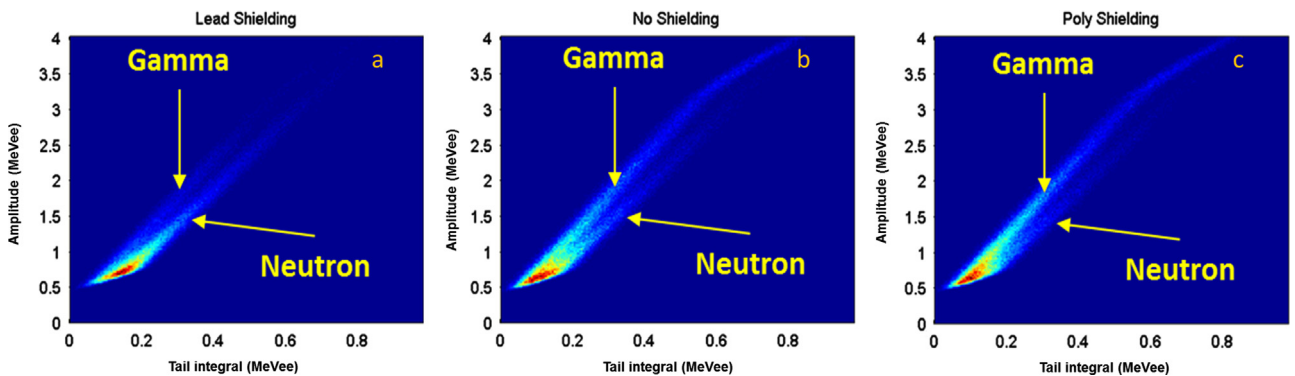
Fig. 7. Illustration of the charge comparison method [17].

Fig. 8. A comparison between a fast neutron pulse and a gamma-ray pulse.

Fig. 9. Tail integral vs. total integral 2D histogram showing PSD performance of the EJ-299-33/SiPM assembly with (a) lead shielding, (b) no shielding and (c) poly shielding.

The FOM value of 0.5426 with a 0.5 MeVee threshold is fairly good for PSD performance. Pozzi et. al. reported a FOM of 0.82 at 120 keVee for EJ-299-33 when coupled with a conventional PMT [6], which is much better than what we observed in this work. We believe the inferior PSD performance is most likely due to the high level of noise introduced by the SiPM array. The longer response time and the effect of the readout circuit may also have contributed to the loss of pulse shape information. Moreover, because the resolution of the oscilloscope is only 8-bit, the digitization process may have also caused some distortion of the pulse shape.

3.3. An investigation of the effect of sampling rate on PSD

In previous sections, the PSD studies were performed using waveforms acquired with a 1 GSPS sampling rate. In many applications, e.g. handheld devices, lower sampling rates are much more commonly used to achieve low system cost and minimal power consumption. Fig. 12(a) and (b) gives an example of the effect of different sampling rates on the digitized waveforms. To investigate the impact of sampling rate on the PSD performance, the originally acquired waveforms were down-sampled to simulate lower sampling rates and the FOM were re-calculated with the same algorithm and parameters. The PSD performance of the EJ-299-33/SiPM array system was re-evaluated with 200 MSPS and 100 MSPS

sampling rates. The results are shown in Fig. 13. A 1.0 MeVee threshold was used. The FOM value was 0.5835 with a 200 MSPS sampling rate, compared to 0.5958 with the original 1GSPS sampling rate. Thus, the PSD performance was comparable. However, when the sampling rate was lowered to 100 MSPS, the PSD performance significantly degraded. The FOM value was only 0.4909, which was 17.6% less than the original value of 0.5958.

The performance degradation at lower sampling rates is due to the notable inaccuracy when choosing the starting point of the charge integration (90% of the maximum on the rising edge) as well as the influence of loss of pulse shape information. The influence could be effectively addressed with upsampling by interpolation before carrying out the PSD analysis. Linear interpolations were performed on the 200 MSPS and 100 MSPS downsampled signals, to bring the effective sampling rate back to 1 GSPS. An example of the pulses after interpolation is shown in Fig. 12(c). The FOM value was then recalculated and the results are
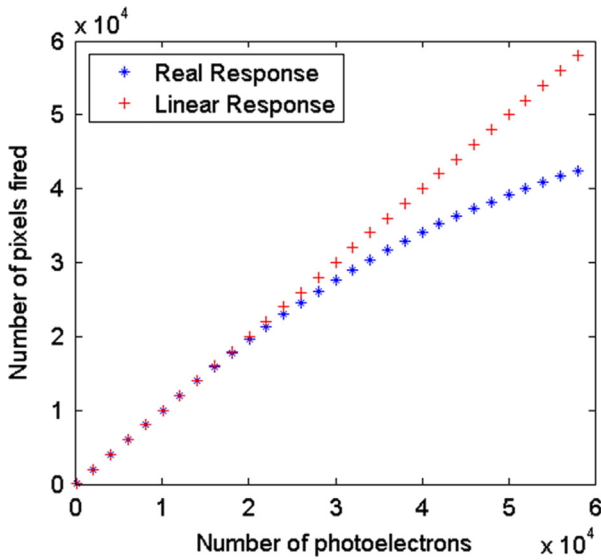

Fig. 12. Waveforms of the original pulse, the pulse downsampled to 100 MSPS and the interpolated pulse.

Fig. 10. Plot of the number of photoelectrons vs. the number of pixels fired compared with a linear response.

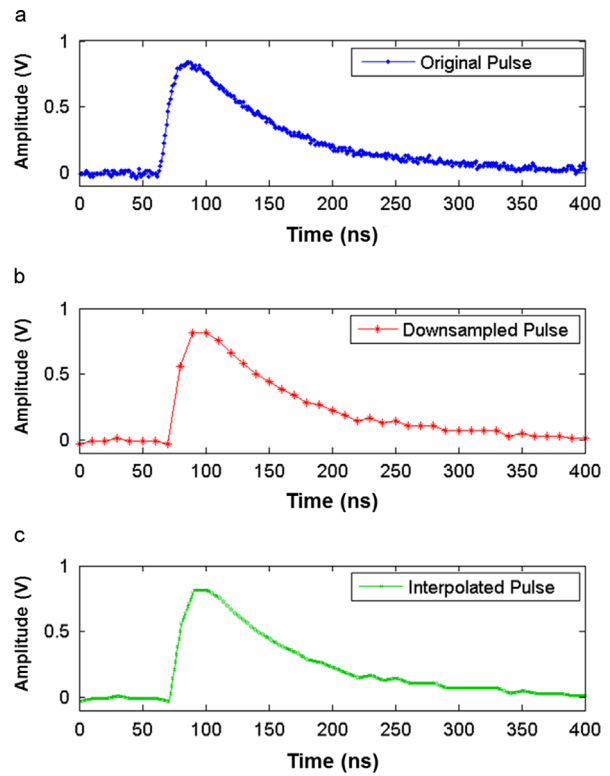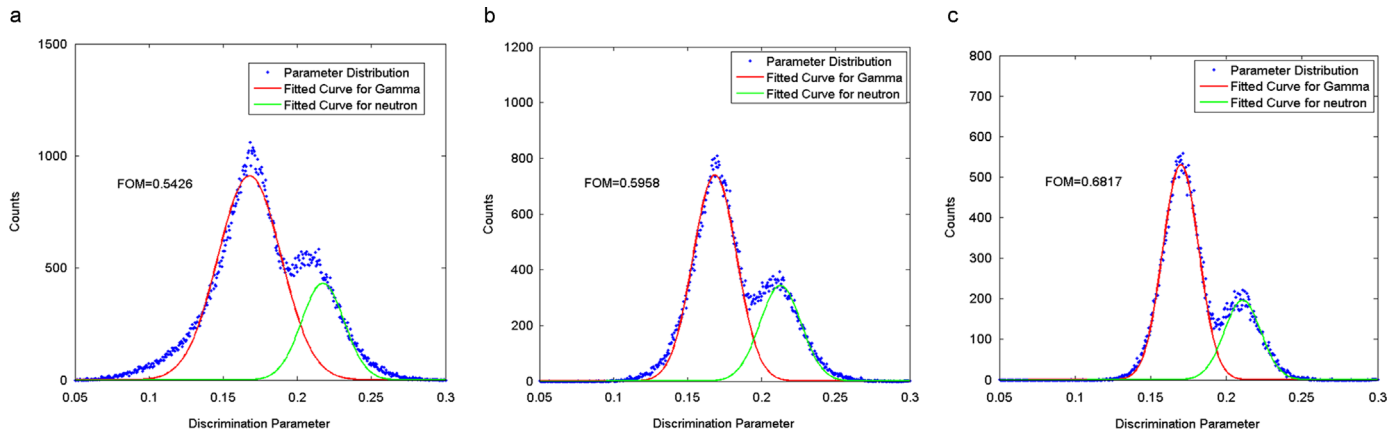**Fig. 11.** Tail-to-total ratio distribution with no shielding, with (a) 0.5 MeVee threshold, (b) 1 MeVee threshold and (c) 1.5 MeVee threshold.
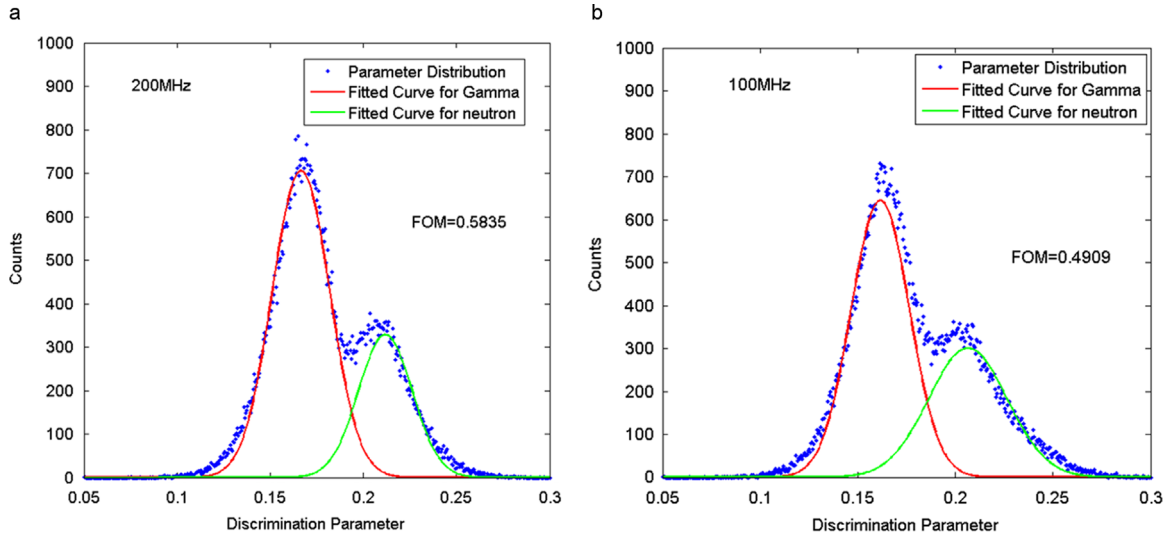
a

b

Fig. 13. Tail-to-total ratio distribution with no shielding, using (a) 200 MSPS and (b) 100 MSPS sampling rates.
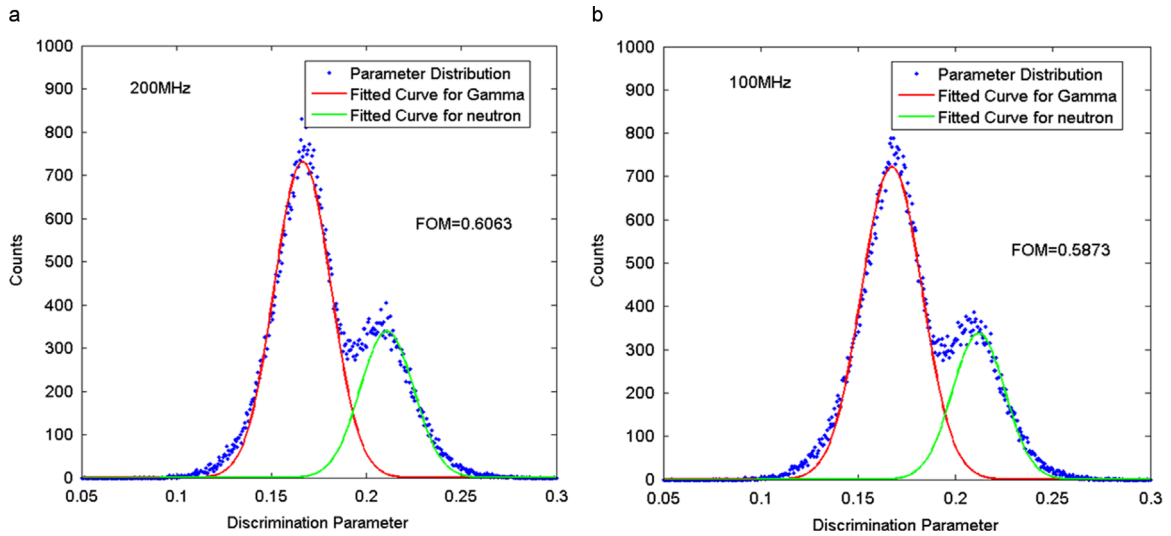
a

b

Fig. 14. Tail-to-total ratio distribution with no shielding (after upsampling by interpolation), using (a) 200 MSPS and (b) 100 MSPS sampling rates.

shown in Fig. 14(a) and (b). As can be observed, the PSD performance is almost identical to what was achieved with the original data. The authors believe that upsampling by interpolation is an effective method to recover the pulse information of a digitized signal to a certain extent. Many other authors have shown similar performance improvement using interpolation [20].

3.4. Frequency gradient analysis method

Frequency gradient analysis (FGA) is a new method proposed by G. Liu. The method increases the FOM by reducing the overlap area between neutron and gamma-ray events. It can be readily implemented in real-time [21]. The FGA method exploits the difference between the Fourier transforms of the neutron pulse and gamma pulse. The Fourier transform takes a time series or a function of continuous time, and maps it onto a frequency spectrum [22]. It takes a function from the time domain and transforms it into the frequency domain which is essentially a decomposition of a function into sinusoids of different frequencies [21]. The discrete Fourier transform (DFT) is used to analyze the digitized signals and the Fast Fourier Transforms (FFT) is a rapid algorithm to compute DFT.
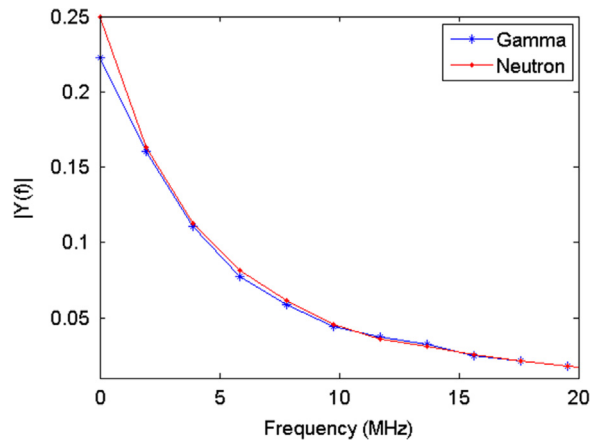

Fig. 15. The magnitude spectra of a neutron pulse and a gamma pulse.

According to Liu's work, extinct differences exist between the magnitude spectra of the gamma pulses and the neutron pulses, especially in the low frequency range. The magnitude spectra of a gamma pulse and a neutron pulse obtained with FFT are illustrated

in Fig. 15. The intersecting regions of the two curves in this case are around 11 MHz and 15 MHz. The magnitude of each frequency component of a neutron pulse is larger than that of a gamma-ray pulse below 11 MHz but slightly smaller between 11 MHz and 15 MHz. Above 15 MHz, the two pulses exhibit almost identical frequency response. The discrimination between neutron and gamma events can then be carried out based on the response difference in the low frequency range below 15 MHz. Thus, the discrimination parameter can be the value of the Fourier transform at zero frequency due to the large discrepancy. However, in order to increase the FOM and to take full advantage of the information provided by Fourier transform, after a few trials, the discrimination parameter was defined as:

$$k = (|Y(0\ MHz)| + |Y(1.953\ MHz)| + |Y(3.906\ MHz)| + |Y(5.895\ MHz)|)/2 - |Y(13.67\ MHz)| \quad (5)$$

where, Y is the FFT result of the pulse.

3.5. PSD results using the FGA method

Using the same data used in Section 3.2, 2D PSD histograms (discrimination parameter k vs. pulse amplitude) for three different shielding configurations are constructed and presented in Fig. 16. The amplitude was calculated using the same integration window described in Section 3.2 to utilize the same energy calibration results obtained in Section 2.2. As observed from the figure, the neutron events and gamma events are better separated using the FGA method than using the charge comparison method.

The distortions in Fig. 16 at large amplitude range are due to the saturation of the pulses above 3.0 MeVee as discussed in Section 3.2.

Before calculating the FOM values, the distortion parts are removed. The FOM with a threshold of 0.5 MeVee is calculated to be 0.6636 based on the discrimination parameter distribution shown in Fig. 17(a). Compared to the value 0.5878 obtained previously using the charge comparison method, the FGA method produced significantly better PSD results. The FOM value is also greater using FGA with 1 MeVee and 1.5 MeVee thresholds. A comparison of the FOM values is shown in Table 1.

The above results indicate that the FGA method produces superior PSD results over the charge comparison method using the same experimental data. As discussed above, the SiPM array exhibits a significant high level of dark current and large noise at room temperature. In the FGA method, the high frequency components of the signal are not utilized for the PSD analysis. We believe this greatly reduces the interference from the high-frequency noise and therefore improved the PSD performance of the detector assembly.

4. Conclusions

The PSD performance of the EJ-299-33 plastic scintillator coupled with a SiPM array from SensL was examined with a PuBe source. Three different shielding configurations were used to alter the relative intensity of neutrons and gamma-rays reaching the detector assembly. A separation of the neutron and gamma events was observed from the experiment results and the best FOM was calculated to be around 0.76 with an energy threshold of 1.0 MeVee. The measurement results illustrated EJ-299-33 coupled with SensL Array-SB is capable of performing PSD. However,
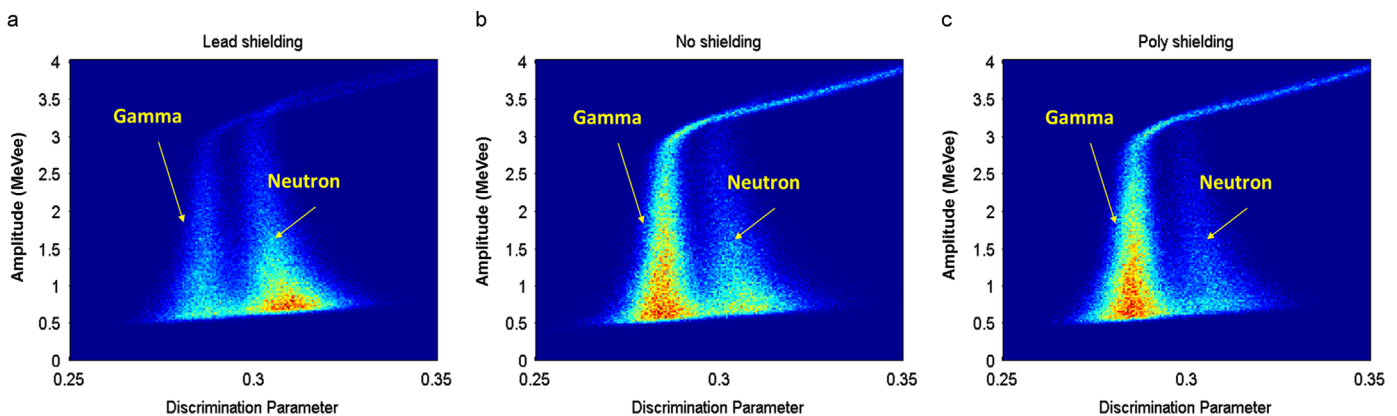

Fig. 16. FGA Discrimination parameter vs. pulse amplitude 2D histogram showing PSD performance of the EJ-299-33/SiPM assembly with (a) lead shielding, (b) no shielding and (c) poly shielding.
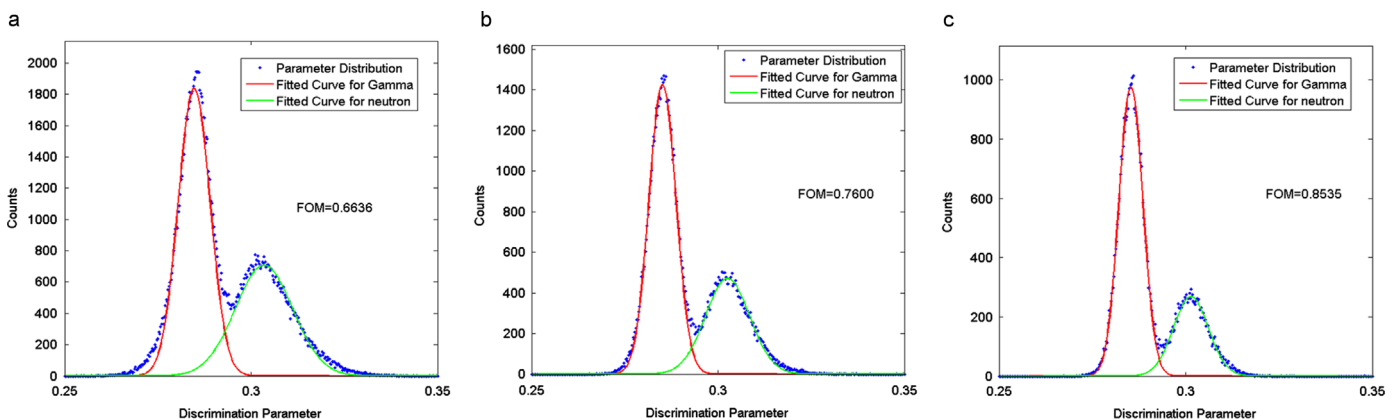

Fig. 17. Discrimination parameter distribution based on FGA method with (a) 0.5 MeVee threshold, (b) 1.0 MeVee threshold and (c) 1.5 MeVee threshold.

Table 1
Comparison between FOM values using FGA and charge comparison methods with different thresholds.

Threshold (MeVee)	FGA	Charge comparison
0.5	0.6636	0.5426
1.0	0.7600	0.5958
1.5	0.8535	0.6817

inferior PSD performance was observed due to the much higher noise level and longer response time of this SiPM array compared with the performance reported using a conventional PMT.

Moreover, the study of the dependence of the PSD quality on the sampling rate showed that the sampling rate does not affect the PSD quality significantly when it was high enough to capture enough pulse shape information. Interpolation technique could be used to recover some loss of information before carrying out the PSD analysis.

A new PSD method, i.e. FGA, was also implemented and compared with the conventional charge comparison method. It exhibited better PSD performance with noisy measurement data. It is our belief that the FGA method is more suitable when SNR of the data is low, such as measurements using SiPM arrays.

For future work, the PSD performance of the new plastic scintillator EJ-299-33 will be studied using SensL C-Series SiPMs, which have a much faster response and a much lower noise level. Results from this study will allow us to evaluate the impact on PSD performance from SiPM noise level and response time. Low-noise SiPMs could potentially provide performance comparable to conventional PMTs while maintaining all the advantages of SSPMs.

References

[1] F.D. Brooks, A scintillator counter with neutron and gamma-ray discrimination, Nuclear Instruments and Methods 4 (1959) 151–163.
[2] G.F. Knoll, Radiation Detection and Measurement, 3rd Ed., John Wiley & Sons, N.J., USA, 2000.
[3] J.B. Birks, The Theory and Practice of Scintillation Counting, Pergamon, London, U.K., 1964.
[4] F.D. Brooks, Development of organic scintillators, Nuclear Instruments and Methods 162 (1979) 477–505.
[5] N. Zaitseva, Plastic scintillators with efficient neutron/gamma pulse shape discrimination, Nuclear Instruments and Methods in Physics Research Section A 668 (2012) 88–93.
[6] S.A. Pozzi, et al., Pulse shape discrimination in the plastic scintillator EJ-299-33, Nuclear Instruments and Methods in Physics Research SectionA 723 (2013) 19–23.
[7] Erika Garutti, Silicon Photomultipliers for high energy physics detectors, Journal of Instrumentation 6 (10) (2011) C10003.
[8] F. Risigo, et al., SiPM technology applied to radiation sensor development, Nuclear Instruments and Methods in Physics Research Section A 607 (1) (2009) 75–77.
[9] I. Tilquin, et al., Detection efficiency of the neutron modular detector DEMON and related characteristics, Nuclear Instruments and Methods in Physics Research A 365 (2–3) (1995) 446–461.
[10] D. Wolski, et al., Comparison of n-γ discrimination by zero-crossing and digital charge comparison methods, Nuclear Instruments and Methods in Physics Research Section A 360 (3) (1995) 584–592.
[11] H. Klein, S. Neumann, Neutron and photon spectrometry with liquid scintillation detectors in mixed fields, Nuclear Instruments and Methods in Physics Research Section A 476 (1–2) (2002) 132–142.
[12] ArraySB-4, scalable, UV-sensitive Silicon Photomultiplier array user manual. ⟨http://www.sensl.com/downloads/ds/UM-ArraySB-4.pdf⟩.
[13] EJ-299-33 plastic scintillator provisional date sheet, Eljen Technology, ⟨http://www.eljentechnology.com/images/stories/Data_Sheets/Plastic_Scintillators/ej299-33%20psd%20data%20sheet.pdf⟩.
[14] Chichester, D. et al. Photon dosimetry using plastic scintillators in pulsed radiation fields, INL/CON-07-12445 (2007).
[15] J.L. Lobdell, N.E. Hertel, Photon spectra and dose measurements using a tissue-equivalent plastic scintillator, Radiation Protection Dosimetry 72 (1997) 95–103.
[16] G. Ranucci, An analytical approach to the evaluation of the pulse shape discrimination properties of scintillators, Nuclear Instruments and Methods in Physics Research Section A 354 (2–3) (1995) 389–399.
[17] C. Liao, H. Yang, n/γ Pulse shape discrimination comparison of EJ301 and EJ339A liquid scintillation detectors, Annals of Nuclear Energy 69 (2014) 57–61.
[18] A. Stoykov, et al., On the limited amplitude resolution of multipixel Geiger-mode APDs, Journal of Instrumentation 2 (2007) P06005.
[19] R.A. Winyard, et al., Pulse shape discrimination in inorganic and organic scintillators. I, Nuclear Instruments and Methods A 95 (1) (1971) 141–153.
[20] F Amorini, et al., Digital signal processing for mass identification in a 4π-detector, using time of flight measurement, IEEE Transaction Nuclear Science 55 (2) (2008) 717–722.
[21] G. Liu, et al., A digital method for the discrimination of neutrons and γ rays with organic scintillation detectors using frequency gradient analysis, IEEE Transaction Nuclear Science 57 (3) (2010) 1682–1691.
[22] J.G. Proakis, D.G. Manolakis, Digital Signal Processing: Principles, Algorithms, and Applications, Prentice-Hall, Upper Saddle River, NJ, 1996, ch. 4.